Large-eddy simulation of the high-Reynolds-number flow through a high-aspect-ratio cooling duct

Thomas Kaller

Technical University of Munich
Department of Mechanical Engineering
Chair of Aerodynamics and Fluid Mechanics
Boltzmannstr. 15, 85748 Garching bei München, Germany
thomas.kaller@tum.de

Vito Pasquariello[1], Stefan Hickel[2] and Nikolaus A. Adams[3]

[1,3] Technical University of Munich
Department of Mechanical Engineering
Chair of Aerodynamics and Fluid Mechanics
Boltzmannstr. 15, 85748 Garching bei München, Germany

[2] Faculty of Aerospace Engineering, Technische Universiteit Delft
P.O. Box 5058, 2600 GB Delft, The Netherlands

ABSTRACT

We present well-resolved large-eddy-simulations (LES) of a straight, high-aspect-ratio cooling duct (HARCD) at a bulk Reynolds number of $Re = 110 \cdot 10^3$ and an average Nusselt number of $Nu = 371$. The geometry and boundary conditions have been defined together with Rochlitz *et al.* (2015), who conducted the experimental measurements for this case. Water was chosen as coolant. The current investigation focuses on the influence of asymmetrical wall heating on the flow field and specifically on the influence of the turbulence-induced secondary flow on turbulent heat transfer, the spatial development of the temperature boundary layer and the accompanying viscosity modulation. Due to the viscosity drop in the vicinity of the heated wall we observe a decrease in turbulent length scales and in turbulence anisotropy, resulting in a decrease of turbulent mixing and the secondary flow strength along the duct.

INTRODUCTION

The turbulent flow and heat transfer in a high aspect ratio (*AR*) duct with rectangular cross section is of great interest for many engineering applications. Examples range from ventilation systems over cooling ducts in motors of hybrid electrical vehicles to the cooling systems of rocket engines. In order to predict the cooling capability and with it the lifetime of the respective system a detailed understanding of cooling duct flows is required.

The turbulent flow through a straight rectangular duct is strongly influenced by the turbulence-induced secondary flow, the so called Prandtl's flow of the second kind. In each duct corner, a pair of counter-rotating streamwise vortices forms as a consequence of the anisotropy of the Reynolds stress tensor. Reynolds-averaged Navier-Stokes (RANS) models based on the isotropic turbulence assumption hence fail to predict these vortices. Even though the secondary flow is relatively weak, $1 - 3\%$ of the bulk velocity, it has a significant influence on momentum and temperature transport and increases the mixing of hot and cold fluid.

Several experimental and numerical studies investigated duct flows of different cross-section. Launder & Ying (1972) studied the flow through adiabatic square ducts with special focus on secondary flows experimentally. The influence of wall heating was analyzed by Wardana *et al.* (1994) for a channel flow. Monty (2005) studied the flow through an adiabatic high-aspect-ratio duct with $AR = 11.7$. Salinas-Vasquez & Métais (2002) performed a first LES of a periodic heated square duct and studied the influence of wall heating on the flow field. Hébrard *et al.* (2005) extended this work to investigate the spatial development of the temperature boundary layer. Choi & Park (2013) analyzed the turbulent heat transfer for rectangular ducts with moderate aspect ratios ranging from $AR = 0.25$ to $AR = 1.5$. Vinuesa *et al.* (2014) presented direct numerical simulations (DNS) of adiabatic periodic duct flows for various aspect ratios ranging from $AR = 1$ to $AR = 7$. All the numerical studies have been conducted at a much lower Reynolds-number than the present study.

In this work, we investigate the influence of asymmetric wall heating on an $AR = 4.3$ duct at a Reynolds-number of $110 \cdot 10^3$ with a moderate temperature difference between coolant and heated wall via LES. We also present a comparison of experimental PIV and the LES results. The main focus of the LES study lies on the effect of wall heating on the turbulence, the secondary flow field and the temperature boundary layer growth.

NUMERICAL MODEL

As only small density variations are present, the flow is described by the incompressible Navier-Stokes equations and the Boussinesq approximation for the gravitational force term. The temperature is treated as an active scalar. The temperature and density dependent thermodynamic properties of the fluid are obtained using the IAPWS correlations, see IAPWS (2008).

The transport equations are discretized by a fractional step finite-volume method on a block structured, staggered Cartesian grid. As time advancement method an explicit third-order Runge-Kutta scheme is applied, while the time-step is adjusted dynamically to maintain a maximum Courant number of 1.0.

For discretizing the pressure Poisson equation and the diffusive

[1] vito.pasquariello@tum.de
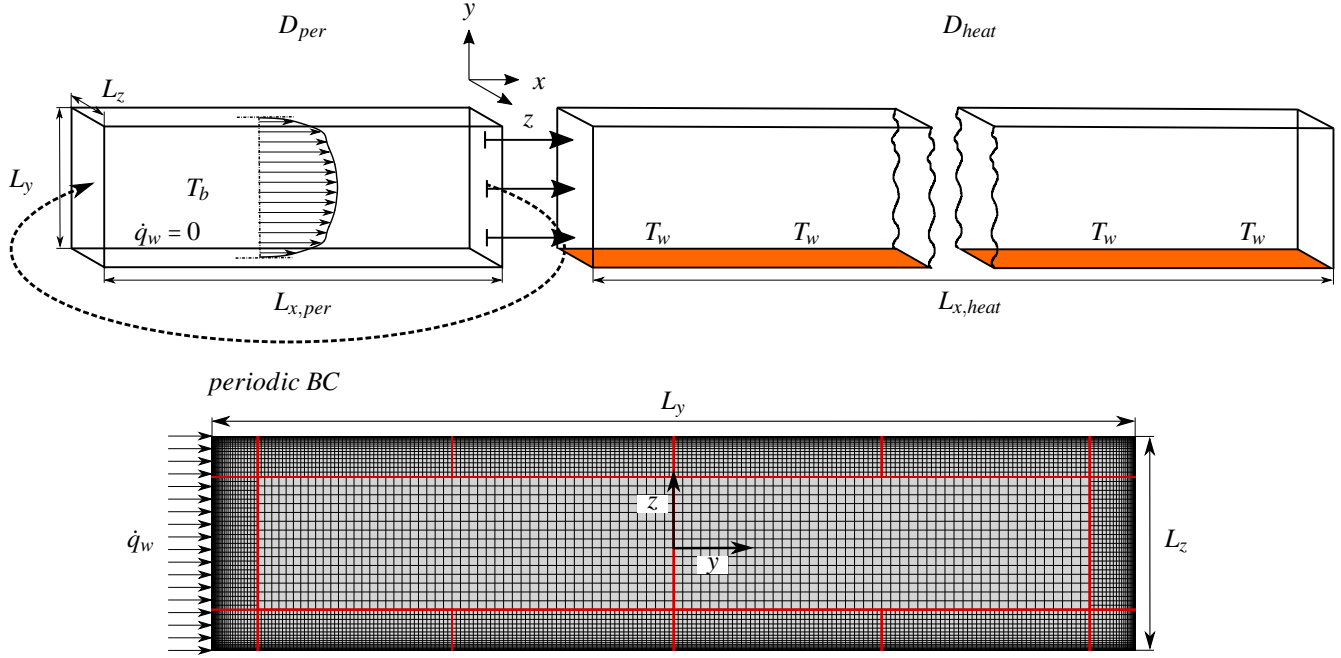[2] s.hickel@tudelft.nl
[3] nikolaus.adams@tum.de

Figure 1: Sketch of the numerical cooling duct setup with periodic domain D_{per} and spatially resolved heated domain D_{heat}. At the bottom the computational grid and blocking in the yz-plane is depicted (every 2nd grid line shown).

fluxes, second-order accurate central difference schemes are implemented. The pressure Poisson equation is solved in every Runge-Kutta substep using a Krylov subspace solver with an algebraic-multigrid preconditioner for convergence acceleration. For discretization of the convective fluxes, the Adaptive Local Deconvolution Method (ALDM) is used, respectively the computationally more efficient simplified SALD method. ALDM is a nonlinear finite volume method that provides a physically consistent subgrid-scale turbulence model for implicit LES, see Hickel *et al.* (2006) and Hickel *et al.* (2014). For the extension and validation for the Boussinesq equations see Remmler & Hickel (2013).

SIMULATION SETUP

The experimental setup of the water cooling duct is constructed as follows. First water at $T_b = 333.15\,\text{K}$ is pumped with a constant flow rate of 50 l/min from a reservoir into a 600 mm unheated feed line. After a flow straigthener the fluid enters into the heated test section of equally 600 mm, where a constant wall temperature of $T_w = 373.15\,\text{K}$ is applied at the lower wall. Both sections are straight ducts of equal cross-section. For further details we refer to Rochlitz *et al.* (2015).

Figure 1 depicts the numerical setup consisting of the adiabatic periodic domain D_{per} and the heated domain D_{heat}. The feed line is modeled as a short periodic duct piece and serves as turbulent inflow generator for the heated duct. For each time-step, the outflow velocity profile of D_{per} is prescribed at the inlet of D_{heat}. At the end of the heated duct, a second-order Neumann boundary condition is applied for velocity and density fluctuations and Dirichlet for pressure.

The duct has a height of $L_y = 25.8$ mm and a width of $L_z = 6$ mm, which results in an aspect ratio of $AR = 4.3$ and a hydraulic diameter of $d_h = 9.74$ mm. The streamwise length of D_{per} is chosen to $L_{x,per} = 7.5 \cdot d_h$ to resolve the large-scale turbulent structures following Vinuesa *et al.* (2014). The heated duct is spatially fully represented with a length of $L_{x,heat} = 600$ mm, corresponding to $61.6\,d_h$. All walls are defined as smooth adiabatic walls except the lower wall of the heated duct section, where the constant tempera-

Table 1: Main flow and simulation parameters.

Re	Nu	Pr_b	$Re_{\tau,y}$	$Re_{\tau,z}$	T_b [K]	T_w [K]
$110 \cdot 10^3$	371	3	4800	5500	333.15	373.15

ture T_w is prescribed.

As initial solution for D_{per} the velocity distribution for a fully developed laminar duct flow superimposed with white noise of amplitude $A \approx 5\% \, u_b$ is defined on a coarse grid. After the state of a fully developed turbulent duct flow is reached, the solution is interpolated onto the fine grid and the simulation continued for several flow-through times (FTT). The final flow state of D_{per} forms the initial condition for the full coupled setup of both flow domains, where D_{heat} is built as a sequence of periodic duct sections. The heating is switched on by setting the isothermal wall temperature to $T_w = 373.15\,\text{K}$. After 1.33 FTT with respect to $L_{x,heat}$ and u_b, statistical sampling is started with a constant temporal sampling interval of $\Delta t_{sample} = 0.025 \cdot (d_h/u_b)$. The sampling extends over 20 FTT. The main flow and simulation parameters are listed in table 1. All Reynolds-numbers are formed using d_h as reference length. The friction Reynolds-numbers are measured in the center of their respective sidewall and represent the adiabatic case. When heating is applied to the lower wall, $Re_{\tau,y}$ increases to 7300. The Prandtl-number is a function of local temperature. The Nusselt-number represents the mean value for the whole domain D_{heat}.

To determine the required grid resolution for a well-resolved LES, an extensive grid sensitivity analysis has been performed for the adiabatic duct. As can be seen in figure 1, a 2:1 connection at the interface of wall blocks and the two inner blocks is applied to reduce the computational cost. The boundary layer blocks possess a hyperbolic grid stretching in the respective wall-normal direction. In the streamwise direction a uniform discretization is applied for all blocks. For $Pr > 1$ thermal length scales are smaller than the mo-

Table 2: Main parameters for grid shown in figure 1.

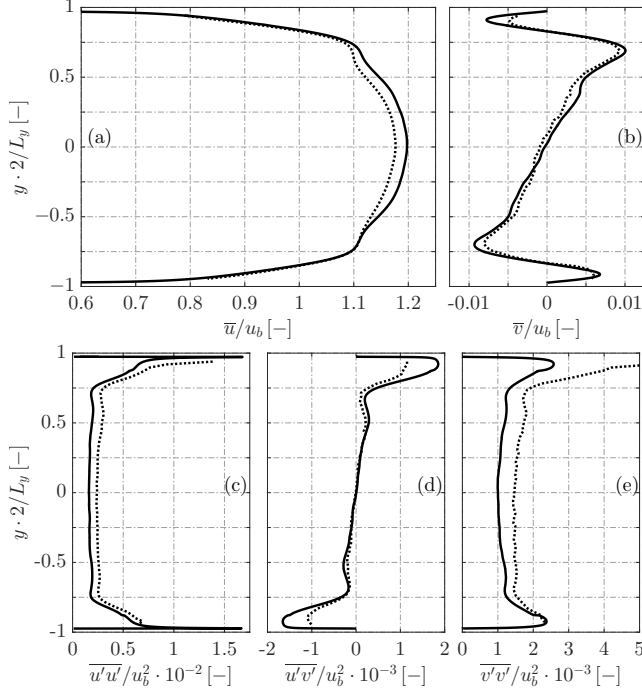|	$D_{per}\|_{lower}$	$D_{per}\|_{upper}$	$D_{heat}\|_{lower}$	$D_{heat}\|_{upper}$
$N_x \times N_y \times N_z$	$576 \times 501 \times 141$	$576 \times 501 \times 141$	$4740 \times 501 \times 141$	$4740 \times 501 \times 141$
$\Delta x^+ \times \Delta y_{min}^+ \times \Delta z_{min}^+$	$62.7 \times 0.73 \times 1.42$	$62.9 \times 1.24 \times 1.42$	$94.5 \times 1.09 \times 1.42$	$62.8 \times 1.24 \times 1.42$
$\frac{\Delta y_{max}}{\Delta y_{min}} \times \frac{\Delta z_{max}}{\Delta z_{min}}$	33.2×27.3	24.2×27.3	33.2×27.3	24.2×27.3

Figure 2: Comparison of experimental (··········) and numerical (———) results for the heated duct. Figures (a)/(b) show the streamwise and heated wall-normal velocity respectively and figures (c)/(d)/(e) the Reynolds stress distribution along the duct center line.

RESULTS
Validation with experimental data

Figure 2 shows the comparison between the LES and the PIV results. An averaging in streamwise direction over the field of view (FOV) ranging from $350 - 400 \, \text{mm}$ and across the laser sheet thickness of $\Delta LS = 1 \, \text{mm}$ is performed. For the latter a constant Gaussian laser intensity distribution along the y-axis is assumed. Due to fabrication tolerances the experimental duct is on average slightly narrower than in the LES leading to a difference in the aspect ratio of $AR_{LES} = 25.8/6.0 = 4.30$ and $AR_{PIV} = 26.1/6.23 = 4.19$ respectively. To account for the different aspect ratio a scaling with respect to the y-axis is performed for the LES data with a factor of AR_{PIV}/AR_{LES}.

For the velocity profile in figure 2 (a) we observe a very good agreement. Until approximately $2y/L_y = \pm 0.75$ the streamwise velocities coincide perfectly. The shoulder section profiles from -0.75 to -0.5 agree well. At the opposite wall larger deviations are present due to the slight asymmetry of the experimental data. The core velocity is slightly higher because of the narrower cross-section, compared to the PIV results $\overline{u}/u_b$ is 1.71% larger. The numerical and experimental $\overline{v}$-profiles also agree well. The peak positions indicating the influence of the corner vortices on the duct center match perfectly. However, the maximum values are again slightly higher. We observe a relatively large deviation for the $\overline{v}$-minimum at the $y = y_{max}$ wall, which we attribute to the aforementioned asymmetry of the experimental data.

The comparison of the Reynolds stresses is depicted in figure 2 (c)/(d)/(e). The streamwise component $\overline{u'u'}$ shows a satisfactory agreement with the LES having consistently lower values than the PIV. This difference is probably due to measurement noise. The coarser grid in the duct core as source of this deviation can be ruled out as an increase of the resolution leads to the same result. The $\overline{u'v'}$ profiles match very well except in the vicinity of the walls, where the LES has higher extrema. The $\overline{v'v'}$ profiles coincide in the vicinity of the heated wall. In the duct center we observe a similar offset like that in $\overline{u'u'}$. At the upper wall large deviations are visible due to an overshoot in the experimental data.

The experimental data exhibits uncertainties with respect to laser sheet misalignment and its effective thickness, so that the latter might be larger than the nominal thickness of $\Delta LS = 1 \, \text{mm}$, which we assumed for postprocessing the LES results. We investigated the influence on the LES data and observed, that both misalignment and an increased ΔLS lead to an improved agreement of LES and PIV.

The flow field of the adiabatic and the heated duct

In the following we analyze the turbulent heat transfer in the asymmetrically heated duct based on the LES results. The main focus lies on investigating the differences of the adiabatic and the heated duct flow field, i.e. on the influence of the wall heating along the duct. As a consequence of the heating, the temperature in the vicinity of the wall increases with the streamwise distance, reducing the local viscosity, which may drop up to $\nu(T_w)/\nu(T_b) = 0.62$.

mentum length scales and the temperature boundary layer is completely contained inside the momentum boundary layer. To resolve the wall-normal temperature gradient, the wall-normal resolution at the heated wall is increased leading to an asymmetric grid with respect to the y-axis. The same mesh is applied for D_{per} and D_{heat} as a matching interface is used.

The main grid parameters for both domains are listed in table 2, separately for the heated lower and the adiabatic upper wall. The number of cells in each direction is denoted by N_x, N_y and N_z leading to $\approx 280 \cdot 10^6$ cells for the discretization of the complete configuration. The dimensionless wall distances of the first respective cell are denoted by Δx^+, Δy_{min}^+ and Δz_{min}^+ and are normalized by the inner length scale $l^+ = \nu_w/u_\tau$ with the friction velocity defined as $u_\tau = \sqrt{\tau_w/\rho_w}$. The quantities are evaluated at the respective wall center. The coarsening ratios $\frac{\Delta y_{max}}{\Delta y_{min}}$ and $\frac{\Delta z_{max}}{\Delta z_{min}}$ relate the largest cell size to the smallest cell size in the boundary layer blocks.
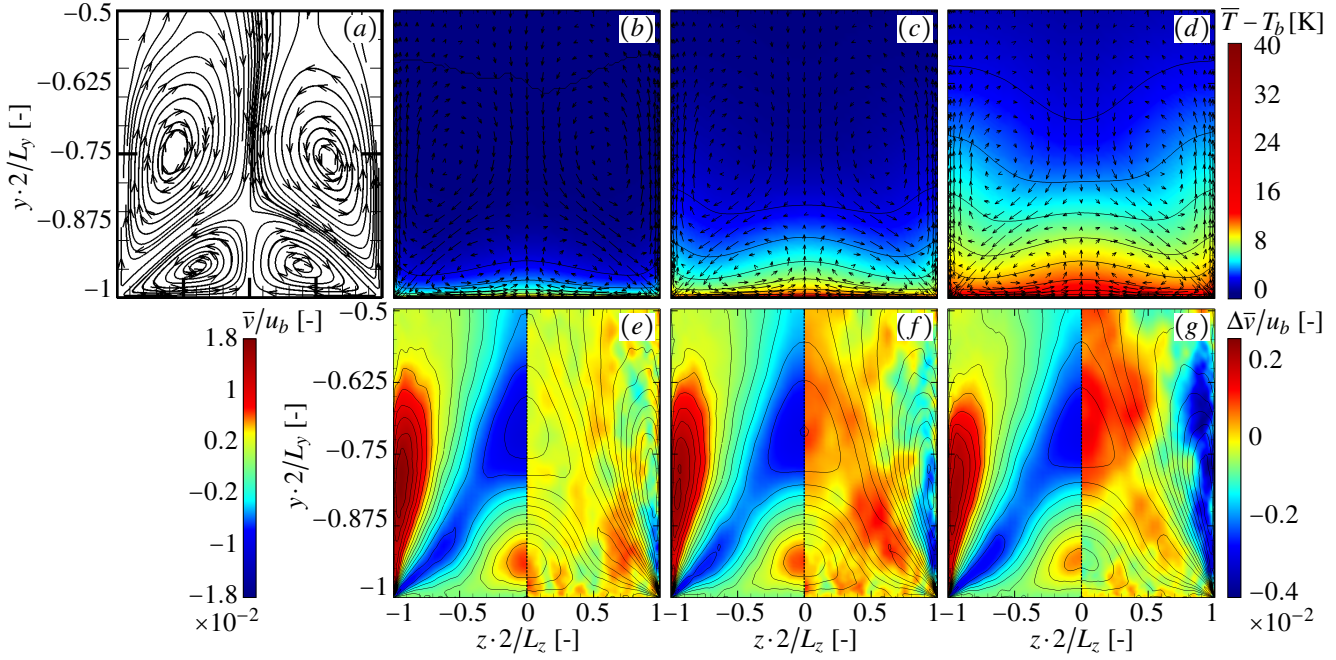
Figure 3: Development of the temperature boundary layer and accompanying change in secondary flow velocity along the duct length in the vicinity of the heated wall. Figure (a) shows the counter-rotating vortices and figures (b)/(c)/(d) the temperature increase at 50 mm, 200 mm and 600 mm respectively. Figures (e)/(f)/(g) depict on the left of the duct center the wall-normal velocity $\bar{v}$ and on the right the change in $\bar{v}$ with respect to the unheated periodic duct, $\Delta\bar{v} = \bar{v} - \bar{v}_{per}$.

The developing temperature boundary layer is highly influenced by the secondary flow structures. Figure 3 (a) shows the pairs of counter-rotating vortices forming in the duct corners. In the left corner, a smaller counter-clockwise (CCW) rotating vortex is forming along the short sidewall and a larger clockwise (CW) rotating vortex along the large sidewall (mirror-inverted for the opposite half of the duct). Each vortex extends to the respective symmetry plane, where it meets the vortex from the opposite side. The vortex strength is relatively weak. The maximum cross-flow velocity for the adiabatic duct is $\bar{u}_{cf}/u_b = \sqrt{\bar{v}^2 + \bar{w}^2}/u_b = 1.93\%$ and lies perfectly within the $1-3\%$ range reported in the literature, see Salinas-Vasquez & Métais (2002). Figures 3 (b)/(c)/(d) depict the axial development of the temperature boundary layer at different positions. The thermal boundary layer thickness increases in streamwise direction due to conduction, turbulent mixing and through transport by the mean secondary flow. The latter is responsible for the characteristic bent shape of the temperature profile. In the left half of the duct, the CW vortex is transporting hot fluid away from the heated wall along the large sidewall into the duct core and cold fluid downwards along the center line. The CCW vortex conveys hot fluid from the corner along the heated wall to its center at $z = 0$ and then upwards along the symmetry line until it mixes with the cold fluid transported downwards. Both vortices push cold fluid into the left corner.

Even though the temperature increase and the accompanying viscosity decrease is relatively moderate, a weakening of the secondary flow strength can be observed in figures 3 (e)/(f)/(g). Depicted is the heated wall-normal secondary flow component $\bar{v}$ at the same spatial positions as the temperature boundary layer plots above. The mean vertical velocity $\bar{v}$ is shown in the left quadrant of each picture and in the right quadrant the difference of the $\bar{v}$-field with respect to the adiabatic case is presented. Comparing $\Delta\bar{v}$ along the heated duct, we observe a significant reduction of the vortex strength. The upward transport of hot fluid in the vicinity of the

large sidewall is slowed down increasingly along the duct length, in the end cross-section at 600 mm the maximum $\Delta\bar{v}/u_b$ is ≈ -0.004 with a velocity of $\bar{v}/u_b \approx 0.015$, which corresponds to a reduction of slightly over 25%. The positions of the vortices remain approximately constant and are defined by the duct geometry. Only for the larger vortex we observe a slight shift in the direction of both sidewalls. As the corner vortices are Reynolds stress induced secondary flows, we will further analyze the influence of the reduced wall viscosity on the turbulence.

In figure 4, we investigate the influence of the wall heating on the turbulent boundary layer in the duct center at $z = 0$ by comparing the adiabatic domain D_{per} with D_{heat}. A spatial averaging is applied, for D_{per} over $L_{x,per} = 7.5 d_h$ and for D_{heat} over the last $7.5 d_h$ of $L_{x,heat}$. For both, the adiabatic and the heated duct, the law of the wall velocity profile is obtained, $u^+ = y^+$ for the viscous sublayer and $u^+ = 1/\kappa \cdot \ln y^+ + B$ for the log-law region. Analogous to Lee *et al.* (2013), we observe in figure 4 (a), that the heating leads to a shift in the log-law region of the velocity profile, the integration constant increases from $B = 5.2$ to $B = 6.0$ for the heated case. The slope and with it the von Kármán constant remains unchanged at $\kappa = 0.41$. Figure 4 (b) depicts the change in the Reynolds stress profiles. The peak in $\overline{u'u'}$ is shifted slightly closer to the wall, whereas the maximum value remains unaltered. Similarly to Zonta *et al.* (2012) the turbulence intensities in all directions are reduced, when heating is applied to the flow. Although counterintuitive, as one would expect an increase in turbulent fluctuations with lower viscosity, this observation is in agreement with previous studies showing that the heating of the fluid leading to a drop in viscosity has a stabilizing effect on the boundary layer, see Lee *et al.* (2013) and Zonta *et al.* (2012).

To analyze the turbulence anisotropy, Banerjee *et al.* (2007) introduced the barycentric map as an extension of anisotropy invariant maps providing a more intuitive visualization technique. The construction is based on the eigenvalues λ_i of the anisotropy tensor of
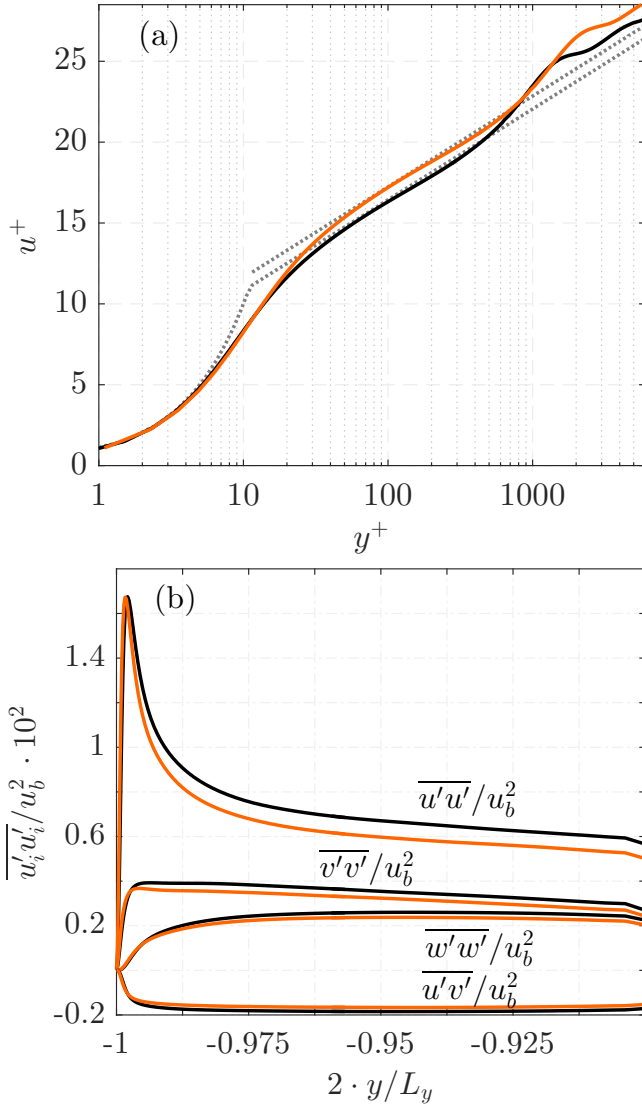
Figure 4: Profiles of (a) mean streamwise velocity and (b) Reynolds stresses along the duct height at $z = 0$ for the adiabatic (——) and the heated duct (——). The law of the wall is represented by (··········).
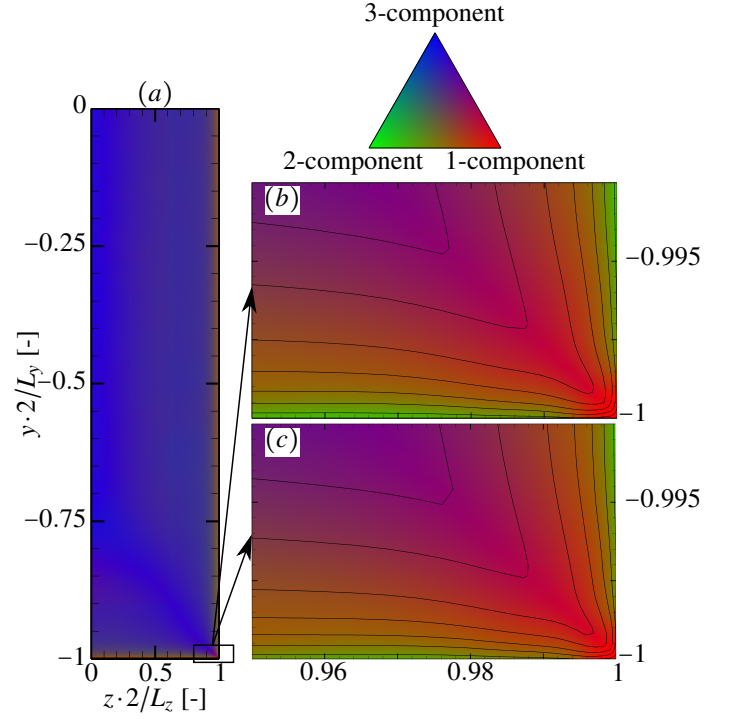

Figure 5: Barycentric anisotropy map illustrating regions of 1-, 2- and 3-component turbulence with (a) adiabatic duct, (b) zoom into the corner and (c) the same view for the heated duct. Isolines signify a constant 3-component fraction.
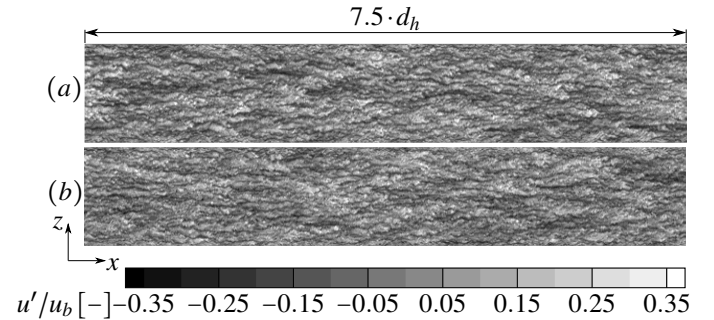

Figure 6: Streamwise velocity fluctuations at the heated wall for (a) adiabatic ($y^+ = 16.1$) and (b) heated duct ($y^+ = 24.2$).

the Reynolds stress tensor and relies on the fact, that any realizable turbulence state can be represented as a combination of the three limiting states of 1-, 2- and 3-component turbulence. The limiting states are defined as the corners of an equilateral triangle with $\mathbf{x}_{1c} = (1, 0)$, $\mathbf{x}_{2c} = (0, 0)$ and $\mathbf{x}_{3c} = (1/2, \sqrt{3}/2)$. The coordinates of a turbulent state are then computed as $\mathbf{x} = C_{1c}\mathbf{x}_{1c} + C_{2c}\mathbf{x}_{2c} + C_{3c}\mathbf{x}_{3c}$ with the weights C_{ic} deduced from λ_i. Finally the coefficient vector C_{ic} is mapped to the RGB triplet. The comparison of the duct corners for the adiabatic and the heated case in figure 5 reveals, that the anisotropy in the vicinity of the heated wall is reduced, in this case the fraction of 2-component turbulence. The flow becomes more isotropic leading to a weaker production term in the streamwise vorticity equation and in turn to a weaker secondary flow.

Figure 6 shows instantaneous streamwise fluctuations in a plane parallel to the heated wall for both the adiabatic and the heated duct. For the latter the last $7.5 d_h$ section is shown. We observe very small turbulent structures as the Reynolds-number is relatively high and hardly any difference between the heated and non-heated result due to the moderate heating. Figure 7 presents streamwise auto-

correlation functions R_{uu}^x taken in the duct center $z = 0$ at different y-locations in the vicinity of the heated wall. For the definition of the longitudinal correlation of the u-velocity we assume local homogeneity in streamwise direction over D_{per} and the last $7.5 d_h$ of the heated duct.

Two observations can be made: first, the structures grow larger with increasing distance from the wall and second, the heating leads to a slight shortening of the turbulent structures. The integral length scale is defined as $L_{uu}^x = \int_0^\infty R_{uu}^x$. In our case we set the upper integration boundary to the point, where the correlation crosses the line $1/e^2$. The heating-induced shortening of L_{uu}^x is listed in table 3. As the temperature increase is highest close to the lower wall, we observe the strongest shortening in L_{uu}^x there with a maximum value of -9.0% for $y^+ = 16.1$. Similarly, the transversal length scales for both streamwise and spanwise velocity reduce with the heating.
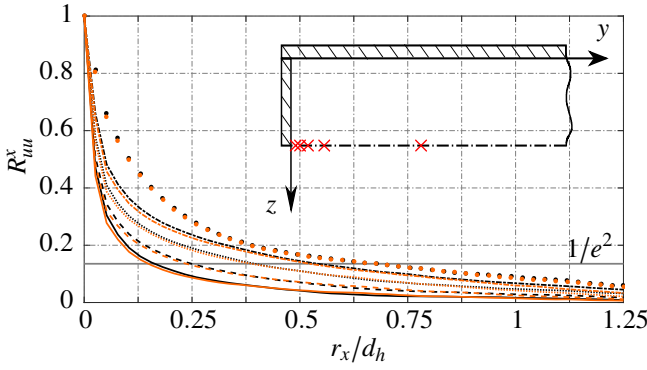
Figure 7: Streamwise autocorrelations of streamwise velocity. Black lines represent the adiabatic and orange ones the heated case. (———) is taken at $y^+ = 16.1$, (- - - - -) at $y^+ = 30.1$, (··············) at $y^+ = 60.5$, (– · – · –) at $y^+ = 120.6$ and (●) at $y^+ = 627.0$. All y^+ values refer to the adiabatic duct.

Table 3: Integral length scales L_{uu}^x and shortening $\Delta_{L_{uu}^x}$.

y^+	16.1	30.1	60.5	120.6	627.0
$L_{uu}^x\|_{per}/d_h \cdot 10^{-2}$	5.1	7.1	10.9	15.3	20.8
$L_{uu}^x\|_{heat}/d_h \cdot 10^{-2}$	4.7	6.7	10.5	14.5	20.6
$\Delta_{L_{uu}^x}$	9.0%	6.3%	4.2%	5.2%	1.2%

CONCLUSION

We investigated the three-dimensional flow field of a straight high aspect ratio cooling duct operated with water at a Reynolds-number of $110 \cdot 10^3$ with an asymmetric wall heating of $\Delta T = 40\,\text{K}$ using a well-resolved LES. Good agreement with experimental PIV measurements by Rochlitz *et al.* (2015) for the same configuration has been achieved for mean velocity and Reynolds stresses.

We analyzed the influence of the turbulence induced secondary flow on the shape of the developing temperature boundary layer along the duct. The counter-rotating vortices forming in each duct corner are relatively weak (the maximum cross-flow velocity is $\approx 2\% u_b$ in our case), but their significant effect on the temperature profile is clearly visible. The temperature rise is accompanied by a drop in viscosity. Even though the heating is relatively moderate, we observed a significant weakening of the strength of the secondary flow along the duct length. As the secondary flow is turbulence-induced, we investigated the effects of the viscosity drop on the near wall turbulence and velocity. In agreement with Zonta *et al.* (2012) and Lee *et al.* (2013), we observed a constant shift of the boundary layer velocity profile and a reduction of turbulence intensity in all directions. Using autocorrelation functions, we quantified the shortening of the turbulent length scales. Applying the barycentric anisotropy map to the flow field, we showed that the turbulence anisotropy in the vicinity of the duct corners is reduced by the heating. The flow becomes more isotropic leading to a weaker production term for streamwise vorticity and a weaker secondary flow.

REFERENCES

Banerjee, S., Krahl, R., Durst, F. & Zenger, Ch. 2007 Presentation of anisotropy properties of turbulence, invariants versus eigen-value approaches. *Journal of Turbulence* **8** (32), 1–27.

Choi, H., S. & Park, T., S. 2013 The influence of streamwise vortices on turbulent heat transfer in rectangular ducts with various aspect ratios. *International Journal of Heat and Fluid Flow* **40**, 1–14.

Hébrard, J., Salinas-Vasquez, M. & Métais, O. 2005 Spatial development of turbulent flow within a heated duct. *Journal of Turbulence* **6**, N8.

Hickel, S., Adams, N. A. & Domaradzki, J. A. 2006 An adaptive local deconvolution method for implicit LES. *Journal of Computational Physics* **213** (1), 413 – 436.

Hickel, S., Egerer, C, P. & Larsson, J. 2014 Subgrid-scale modeling for implicit large eddy simulation of compressible flows and shock-turbulence interaction. *Physics of Fluids* **26** (106101).

IAPWS 2008 Release on the IAPWS Formulation 2008 for the Viscosity of Ordinary Water Substance. available from http://www.iapws.org.

Launder, B., E. & Ying, W., M. 1972 Secondary flows in ducts of square cross-section. *Journal of Fluid Mechanics* **54** (2), 289–295.

Lee, J., Yoon Jung, S., Jin Sung, H. & Zaki, T. A. 2013 Effect of wall heating on turbulent boundary layers with temperature-dependent viscosity. *Journal of Fluid Mechanics* **726**, 196–225.

Monty, J. P. 2005 Developments In Smooth Wall Turbulent Duct Flows. PhD thesis, The University of Melbourne.

Remmler, S. & Hickel, S. 2013 Spectral structure of stratified turbulence: Direct numerical simulations and predictions by large eddy simulation. *Theoretical and Computational Fluid Dynamics* **27** (3-4), 319–336.

Rochlitz, H., Scholz, P. & Fuchs, T. 2015 The flow field in a high aspect ratio cooling duct with and without one heated wall. *Experiments in Fluids* **56** (12), 1–13.

Salinas-Vasquez, M. & Métais, O. 2002 Large-eddy simulation of the turbulent flow through a heated square duct. *Journal of Fluid Mechanics* **453**, 201–238.

Vinuesa, R., Noorani, A., Lozano-Duran, A., El Khoury, G., Schlatter, P., Fischer, P., F. & Nagib, N., M. 2014 Aspect ratio effects in turbulent duct flows studied through direct numerical simulation. *Journal of Turbulence* **15** (10), 677–706.

Wardana, I. N. G., Ueda, T. & Mizomoto, M. 1994 Effect of strong wall heating on turbulence statistics of a channel flow. *Experiments in Fluids* **18** (1), 87–94.

Zonta, F., Marchioli, C. & Soldati, A. 2012 Modulation of turbulence in forced convection by temperature-dependent viscosity. *Journal of Fluid Mechanics* **697**, 150–174.